Earth and Planetary Science Letters 528 (2019) 115842

Contents lists available at ScienceDirect

Earth and Planetary Science Letters

www.elsevier.com/locate/epsl

Revisiting erosion rate estimates from luminescence profiles in exposed bedrock surfaces using stochastic erosion simulations

N.D. Brown[a,b,c,*], S. Moon[a,**]

[a] Department of Earth, Planetary, and Space Sciences, University of California, Los Angeles, CA, USA
[b] Department of Earth and Planetary Sciences, University of California, Berkeley, CA, USA
[c] Berkeley Geochronology Center, 2455 Ridge Road, Berkeley, CA, USA

ARTICLE INFO

Article history:
Received 20 February 2019
Received in revised form 28 August 2019
Accepted 11 September 2019
Available online xxxx
Editor: R. Bendick

Keywords:
OSL
exposure dating
erosion rate
rock surface
bias
luminescence

ABSTRACT

Exposed bedrock is ubiquitous on terrestrial and planetary landscapes, yet little is known about the rate of granular-scale bedrock erosion on timescales longer than the instrumental record. As recently suggested, using the bleaching depth of luminescence signals as a measure of bedrock erosion may fit these scales. Yet this approach assumes constant erosion through time, a condition likely violated by the stochastic nature of erosional events. Here we simulate bedrock luminescence bleaching in response to power-law distributions of removal lengths and hiatus durations. We compare simulation results with previously measured luminescence profiles from boulder surfaces (Sohbati et al., 2018) to illustrate that prolonged hiatuses are unlikely and that typical erosion scales are sub-granular with occasional loss at mm scales, consistent with ideas about microflaws governing bedrock detachment. For a wide range of erosion rates, measurements are integrated over many removal events, producing reasonably accurate estimates despite the stochastic nature of the simulated process. We hypothesize that the greater or equal erosion rates atop large boulders compared to rates at ground level suggest that subcritical cracking may be more influential than aeolian abrasion for boulder degradation in the Eastern Pamirs, China.

1. Introduction

Bare bedrock appears across Earth's surface when the rate of rock degradation by chemical and physical weathering is slow compared to the rate of debris removal by physical erosion. In these weathering-limited regimes, bedrock erosion can set the pace for landscape evolution (Gilbert, 1877; Portenga et al., 2013). On subdecadal timescales, rock surface lowering has been measured using micro-erosion meters (Spate et al., 1995) and remote sensing methods (Moses et al., 2014). Occasionally, erosion can be measured relative to a known-age historic datum (Emmanuel and Levenson, 2014). On timescales of $> 10^4$–10^6 a and spatial scales of several decimeters to several meters, cosmogenic nuclide (CN) concentrations provide erosion rate estimates from exposed bedrock (Small et al., 1997; Bierman and Caffee, 2002; Portenga and Bierman, 2011). Yet few techniques quantify erosion rates at the spatial scale of individual mineral grains and timescales of centuries to millennia.

Recently, Sohbati et al. (2018) have shown that the bleaching depth of luminescence signals in bedrock should reflect either the apparent time since daylight exposure (Sohbati et al., 2011) or the apparent erosion rate ($\sim 10^{-2}$–10^{3} mm·a^{-1}), analogous to the use of in situ CN concentrations in bedrock surfaces (Lal, 1991; Granger and Riebe, 2014). This technique is sensitive to timescales of $\sim 10^2$–10^4 a and spatial scales of mm to cm, thereby providing a unique tool for erosion-rate studies that can bridge the gap between shorter- and longer-timescale methods (Sohbati et al., 2018).

This method assumes a constant erosion rate through time, yet several observations suggest that the erosion of subaerially exposed bedrock is likely to be stochastic in nature. Climatic variables such as temperature and precipitation are known to influence chemical weathering (Perron, 2017), fracture propagation (Eppes and Keanini, 2017), aeolian abrasion via sand availability and wind intensity (Bridges and Laity, 2013), and biotic activity (Viles, 2012). Climatic variability may therefore produce irregularity in the rate of bedrock degradation.

Irregularities in erosion magnitude or frequency are known to cause bias in measurements of geomorphic systems (Gardner et al., 1987). For example, false increases in erosion rate through time

---

* Corresponding author at: Department of Earth and Planetary Sciences, University of California, Berkeley, CA, USA.
** Corresponding author.
E-mail addresses: nathan.brown@berkeley.edu (N.D. Brown), sgmoon@ucla.edu (S. Moon).

https://doi.org/10.1016/j.epsl.2019.115842

have been observed for fluvial incision in bedrock (Finnegan et al., 2014) and glacial landscape erosion (Ganti et al., 2016), both resulting from a heavy-tailed distribution of erosional hiatuses, analogous to the apparent increase in sedimentation that results from a distribution of depositional hiatuses (Sadler, 1981; Schumer and Jerlomack, 2009). Large, rare erosional events can also lead to measurement bias, as observed when basin-averaged erosion rates are influenced by landslides (Niemi et al., 2005). A time-dependence on rate measurements has been proposed when the magnitude of these events belongs to a heavy-tailed distribution (Yanites et al., 2009). Similarly, short-term erosion rates (e.g., sediment flux, reservoir accumulation) will likely underestimate the long-term rates if they fail to include large but rare catastrophic erosional events (Kirchner et al., 2001). These effects illustrate a common principle, that whether or not extreme hiatuses or erosion events are included in an erosion rate measurement can significantly alter the interpretation (Finnegan et al., 2014; Ganti et al., 2016). At the spatial scale relevant to luminescence measurements, anomalously high erosion might result from the occasional detachment of grains (Spate et al., 1995) or rock fragments (Eppes and Keanini, 2017), while a prolonged hiatus might follow a shift in climatic conditions (Bridges et al., 2004).

In this study, we investigate how the apparent erosion rate measured from a luminescence depth profile compares with the erosion rate from simulations of stochastic erosion. The length of material removed in individual erosional events and the time interval between these events are randomly sampled from power-law distributions, similar to previous investigations of how episodic spallation influences CN-derived erosion rates (Small et al., 1997; Muzikar, 2008, 2009). We use this approach to interpret the accuracy of, and the erosional conditions implied by, the previously published dataset of Sohbati et al. (2018). We define the critical length- and time-scales which control accuracy when estimating power-law erosion rates. Finally, we describe how this approach can provide insights into the dominant mechanisms of bedrock erosion on centennial-to-millennial timescales.

2. Theoretical background

The depth of the luminescence bleaching front propagates down into a recently-exposed bedrock surface logarithmically with time until an equilibrium is reached between charge detrapping due to daylight bleaching and charge trapping due to geologic irradiation (Sohbati et al., 2012). For a non-eroding surface, Eq. (4) of Sohbati et al. (2018) describes the fractional saturation n/N of traps as a function of both depth x (mm) and time t (ka):

$$\frac{n(x,t)}{N} = \frac{E(x)\exp[-t(E(x)+F)]+F}{E(x)+F} \tag{1}$$

$E(x)$ is the detrapping rate (ka^{-1}) at a given depth, which depends on the exposure-time-averaged detrapping rate at the rock surface $\overline{\sigma\phi_0}$ (ka^{-1}) and the inverse of the photon mean free path μ (mm^{-1}) as follows:

$$E(x) = \overline{\sigma\phi_0}\exp(-\mu x) \tag{2}$$

F is the trapping rate (ka^{-1}), treated as equal for all depths and dependent upon the geologic dose-rate $\dot{D}$ (Gy·ka^{-1}) and the characteristic dose D_0 (Gy):

$$F = \dot{D}/D_0 \tag{3}$$

In Fig. 1a, we illustrate the bleaching profile for a non-eroding surface in terms of the depth which is half bleached relative to field saturation $x_{0.5}$ for times ranging from 1 a to 1 Ma, using the same sample parameters as in Fig. 1 of Sohbati et al. (2018): $\mu = 0.6$ mm^{-1}, $\overline{\sigma\phi_0} = 2200$ ka^{-1}, $D_0 = 250$ Gy, $\dot{D} = 6$ Gy·ka^{-1}. Eventually, $x_{0.5}$ will reach a steady-state depth d_{SS}, which can be solved for by setting $n/N = 0.5$ and letting t approach infinity in Eq. (1):

$$d_{SS} = -\ln\left(\dot{D}/\left[D_0 \cdot \overline{\sigma\phi_0}\right]\right)/\mu \tag{4}$$

A profile with a $x_{0.5}$ depth that is indistinguishable from this zero-erosion, steady-state depth d_{SS} cannot provide a finite age or erosion rate.

Under constant erosion, however, the bleaching depth $x_{0.5}$ will reach a dynamic equilibrium that is closer to the surface ($x_{0.5} < d_{SS}$) due to the continuous lowering of the bleached overburden rock. In this case, the equilibrium bleaching profile can be described as

$$\frac{n(x,\dot{\varepsilon})}{N} = M\left(1, 1+\frac{F}{\mu\dot{\varepsilon}}, -\frac{E(x)}{\mu\dot{\varepsilon}}\right) \tag{5}$$

where M is the confluent hypergeometric function (Sohbati et al., 2018).

In this case, the luminescence bleaching profile yields an erosion rate and the apparent exposure age is interpreted as the averaging time t_{avg} (Fig. 1; cf. Fig. 6b of Sohbati et al., 2018). For example, if a luminescence profile could be interpreted as either an exposure age of 8.8 ka (using Eq. (1)) or an erosion rate of 0.15 mm·ka^{-1} (using Eq. (5)), the latter would be interpreted as an erosion rate averaged over the past 8.8 ka.

Due to experimental limitations, finite erosion rates can be mistakenly inferred from zero-erosion steady-state profiles. Therefore, Sohbati et al. (2018) defined the depth $d_{SS} - 1/\mu$ as the sample-specific limit on the lowest resolvable constant erosion rate and the uppermost averaging timescale (see purple dashed lines in Fig. 1). In this study, because our accuracy assessments are not limited by empirical uncertainties, and because measurement capabilities are likely to improve (e.g., Sellwood et al., 2019), we use a threshold of $0.99 * d_{SS}$ to limit the lowest resolvable erosion rate.

Critically, a bleaching depth $x_{0.5}$ will yield an apparent erosion rate regardless of whether the assumptions required by Eq. (5) are met. For example, Fig. 2 illustrates how bleaching profiles sampled at three separate locations on a single rock might vary due to irregular erosional histories. Any of these profiles could be used to calculate an apparent erosion rate (Fig. 1b), but none of those rates would represent a long-term constant erosion rate. Likewise, a rock surface may experience constant erosion at a low rate for a period of time before undergoing some higher constant rate. If such a rock were sampled soon after that moment of transition, the assumption of constant erosion rate would be valid, but the luminescence bleaching profile would still be in the process of migrating to re-equilibrate with the surficial erosion rate. The time required to equilibrate with the new erosion rate would depend on the difference between the two rates as well as the luminescence properties of the rock.

Because the assumption of constant erosion over the averaging time cannot typically be guaranteed in nature, we label an erosion rate estimated from a bleaching profile as an apparent erosion rate. In this study, apparent erosion rates are inferred either from measured or simulated luminescence profiles, labeled $\dot{\varepsilon}_A^M$ and $\dot{\varepsilon}_A^S$, respectively. Conversely, we define the true erosion rate $\dot{\varepsilon}_T^S$ at a certain simulation time t_i as the total removed length in the preceding t_{avg} years (Fig. 4):

$$\dot{\varepsilon}_T^S(t_i) = \frac{1}{t_{avg}} \sum_{t=t_i-t_{avg}}^{t_i} l(t) \tag{6}$$

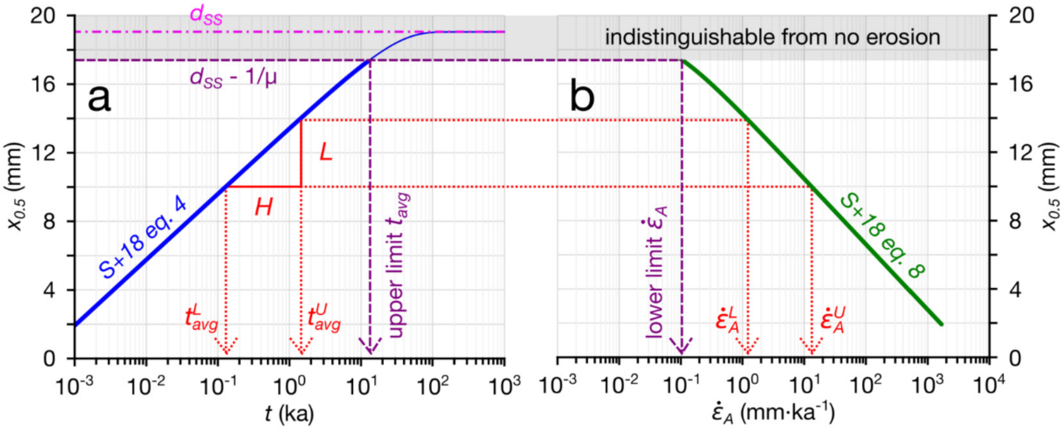

Fig. 1. (a) If the erosional period H and removal length L are unchanging, $x_{0.5}$ will oscillate within the portion of the $x_{0.5}(t)$ curve where $dt = H$ and $dx_{0.5} = L$. (b) At any moment in time, the $x_{0.5}$ value will yield an apparent constant erosion rate $\dot{\varepsilon}_A$. These curves are defined as Eqns. 4 and 8 in Sohbati et al. (2018). The t_{avg} value for $\dot{\varepsilon}_A$ will fall within the zone shown in (a) where superscripts L and U represent lower and upper bounds. The bleaching depth that is indistinguishable from no erosion, shown in gray, defines the lower limit of resolvable erosion rates and also the longest averaging time that can be measured. (For interpretation of the colors in the figure(s), the reader is referred to the web version of this article.)

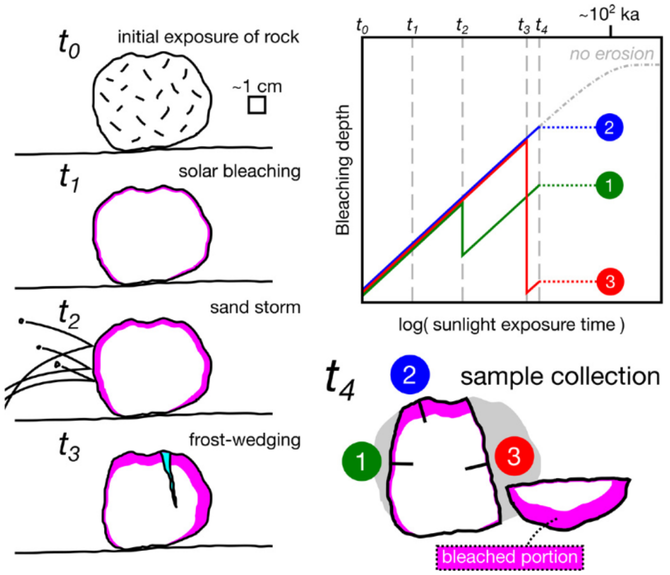

Fig. 2. Example of how the bleaching profile of a rock may evolve in response to several erosional events. From initial bedrock exposure at time t_0 until the eventual sample collection at t_4, different surfaces on the same cobble may develop different luminescence bleaching profiles in response to discrete removal events. The plot in the upper-right corner illustrates how the bleaching depth (e.g., $x_{0.5}$) of collection points 1–3 evolve over time following exposure and erosion. The dash-dotted gray line shows the bleaching depth without erosion.

By defining the true erosion rate in this way, we are able to evaluate the performance of Eq. (5) by mimicking the steps that a geologist would take: first determining the bleached depth $x_{0.5}$, then calculating the corresponding erosion rate $\dot{\varepsilon}^S_A$ and averaging timescale t_{avg} using Eqs. (5) and (1), respectively. We then use the known history of removal lengths l_i and hiatus durations h_i to calculate the true erosion rate $\dot{\varepsilon}^S_T$ during t_{avg}.

When a profile reaches dynamic equilibrium, the erosion rate will be equal to the rate of change of $x_{0.5}$, i.e.

$$\partial x_{0.5}/\partial t = \dot{\varepsilon}_A \tag{7}$$

Only when these two rates are equal will the bleaching depth $x_{0.5}$ be constant through time. This allows us to relate time and length scales directly to sample-specific erosion rates.

3. Methods

To investigate how inconstant erosion affects a bleaching profile (and therefore an erosion rate estimate), first we consider periodic erosion: after some fixed hiatus H, a given length L is removed from the bedrock surface and the bleaching depth reduces by this length or goes to zero. Hereafter, we summarize the luminescence bleaching profile as the depth where luminescence intensity is half of saturation intensity, $x_{0.5}$. After several removal cycles, a dynamic balance will be reached when the increase in $x_{0.5}$ that occurs during H is equal to L (Figs. 1 and 3). When the averaging time t_{avg} is greater than some multiple n of H, the true erosion rate will be $(n \cdot L)/t_{avg}$. The number of removal events included in a measurement is of the order $(\mu L)^{-1}$, where μ is the light attenuation coefficient (mm^{-1}). Our approach is similar to previous studies that have examined how the episodic removal of surface material influences CN-derived estimates of erosion rate (Small et al., 1997; Muzikar, 2008, 2009).

Next, we model stochastic erosion by randomly sampling both the removal length and the time between removal events from power-law distributions. The power law distributions from which l and h values are sampled are defined as

$$p(\theta) = \theta^{-\alpha} \cdot (\alpha - 1)\, \theta_{min}^{\alpha-1} \tag{8}$$

where θ is the continuous random variable, θ_{min} is the minimum value for which the power law applies and α is the tailing factor which controls the relative probability of greater values so that $p(\theta) \propto \theta^{-\alpha}$ (Fig. 3) (Clauset et al., 2009). Each randomly chosen instance of $\theta = l$ or $\theta = h$ in Eq. (8) was generated using the following expression

$$\theta = \theta_{min} \cdot (1 - r)^{-1/(\alpha-1)} \tag{9}$$

where r is sampled from a uniform random distribution where $0 \le r < 1$ (Clauset et al., 2009). Notice that α relates to the Pareto distribution tailing factor, β (e.g., Schumer and Jerlomack, 2009; Ganti et al., 2016), as $\alpha = \beta + 1$. The median values of these distributions $\widetilde{\theta}$ are defined as

$$\widetilde{\theta} = \theta_{min} \cdot 2^{1/(\alpha-1)} \tag{10}$$

following Clauset et al. (2009).

We simulated 1026 unique, 150-ka-long erosional histories for each of the 8 samples analyzed in Sohbati et al. (2018). The first

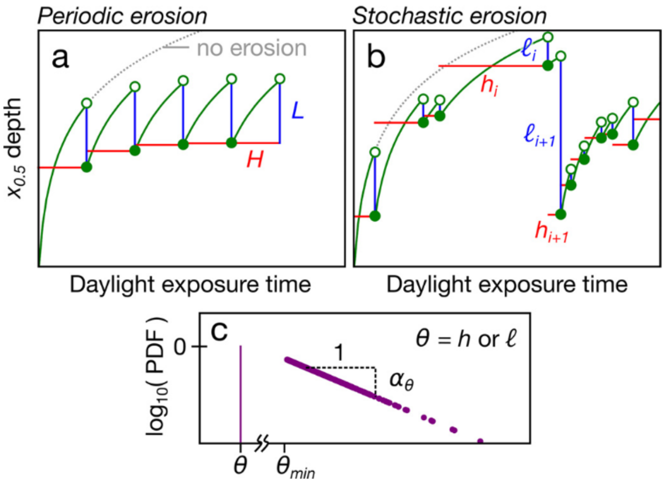

Fig. 3. The evolution of bleaching depth $x_{0.5}$ with daylight exposure time and (a) periodic or (b) stochastic erosion. During periodic erosion, the bleaching front comes closer to the surface after each removal event, shown as empty and filled circles, until a dynamic balance is reached where the additional bleaching depth during the period between removals H is equal to the removal length L. Under stochastic erosion, no such balance is reached. The dotted gray line shows the case of no erosion. (c) The probability density functions for hiatus and removal length inputs for stochastic erosion simulations (see Eq. (8)), where the horizontal axis is logarithmic.

50 ka and final 1 ka of each simulation were omitted from further analysis to allow the bleaching depth to evolve in response to removal events and to eliminate boundary condition effects (Ganti et al., 2016) for a total considered history of 99 ka per iteration. Both α_L and α_H were allowed to vary between 1.1 and 3 (Schumer and Jerlomack, 2009; Ganti et al., 2016). For the tailing factors, α_L and α_H, values ≤ 1 are not defined, values between 1 and 2 result in heavy-tailed distributions and values ≥ 2 produce thin-tails, similar to exponential decay (Clauset et al., 2009), as has been observed, for example, with sand-transport capacity during wind storms (Jerolmack et al., 2011). The minimum (i.e., most probable) removal length l_{min} was allowed to vary from to 0.1 µm to 10 cm, a range that encompasses field (Spate et al., 1995) and experimental observations of chipping caused by grain impact (Wright et al., 1998) or subcritical cracking (Eppes et al., 2016; Eppes and Keanini, 2017). For minimum hiatus duration h_{min}, possible values ranged from 1 a to 100 a (simulation $dt = 0.1$ a). Weather station measurements from 1982 to 2007 suggest that wind storms occur in this region with a frequency of $0 - 1$ a^{-1} (Song et al., 2016).

In response to each prescribed erosion history, several values were calculated at every time step using Eqs. (1), (5), and (6). By setting $n/N = 1/2$ in Eq. (1), the bleaching depth $x_{0.5}$ is determined throughout each hiatus duration h_i. At the end of each hiatus, the erosion event will reduce the $x_{0.5}$ depth by some removal length l_i. From this updated $x_{0.5}$ value, an apparent age (Eq. (1)) and an apparent erosion rate $\dot{\varepsilon}_A^S$ (Eq. (5)) can be calculated (Fig. 1). Notice that the apparent age is interpreted as the averaging time for the apparent erosion rate, t_{avg} (Sohbati et al., 2018). Lastly, the true erosion rate is calculated as the summed removal lengths averaged over the preceding t_{avg} time period (Eq. (6)).

A representative simulation of stochastic erosion is shown in Fig. 4. Two phenomena are notable. First, the true erosion rate drops abruptly when a large removal event occurred just prior to the averaging time and is not included in the true erosion rate calculation (Eq. (6)), as shown in the yellow highlighted region. Unlike the apparent erosion rate, the true rate is highly sensitive to whether or not unusually large events occurred within the averaging time (Fig. 4j). Second, during a hiatus, the ratio of $\dot{\varepsilon}_A^S/\dot{\varepsilon}_T^S$ decreases. This happens because $\dot{\varepsilon}_A^S$ decreases faster than $\dot{\varepsilon}_T^S$ (Fig. 5d).

4. Results

4.1. Estimating erosion and hiatus characteristics from luminescence profiles

Based on the simulations of stochastic erosional processes, we show the distributions of removal length and hiatus duration that are likely to produce the measured erosion rates in Fig. 6. The number of time steps where $\dot{\varepsilon}_A^S = \dot{\varepsilon}_A^M \pm 2\sigma$ is divided by the total number of time steps for each simulation, and the maximum overlap ratios are shown according to the simulation conditions in Figs. 6 (h_{min} vs. l_{min} and α_H vs. α_H) and S1 (h_{min} vs. α_H and l_{min} vs. α_L). For example, in Fig. 6e, the measured erosion rate for sample Muztagh-2-1 would have been measured about 80% of the time in a simulation that imposed h_{min} and l_{min} values of about 1 µm and 3 a, respectively. The erosional conditions producing maximum overlap ratio of $\dot{\varepsilon}_A^S$ and $\dot{\varepsilon}_A^M \pm 2\sigma$ are considered most probable and are listed in Table S2.

Samples XJ64 and XJ64-1 represent the maximum and minimum $\dot{\varepsilon}_A^M$ values: 444 ± 12 and $< 0.038 \pm 0.002$ mm·ka^{-1}, respectively. Both were sampled from the same location atop a glacial moraine in the Kuzigun valley (Owen et al., 2012); XJ64 was taken from the top of a large (>2 m diameter) boulder and XJ64-1 from the exposed surface of a partially buried boulder, a few cm above the ground. Unsurprisingly, the erosion rate measured for XJ64-1 ($\dot{\varepsilon}_A^M = 0 - 0.04$ mm·ka^{-1}) can be reproduced under most conditions. The only conditions that fail to frequently produce this rate are frequent, heavy-tailed removals (Fig. 6i). By contrast, even by allowing l_{min} values as large as 1.7 ± 1.6 cm, the erosion rate observed for XJ64 was only reproduced 7% of the time in the simulation with the most overlapping time steps (Fig. 6h). While α_L could vary among likely scenarios, α_H was uniformly large (Fig. 6p). This suggests that prolonged erosional hiatuses are unlikely to produce the large $\dot{\varepsilon}_A^M$ value from XJ64.

The remaining six samples, which yield measured erosion rates between 0.09 and 1.72 mm·ka^{-1}, are reproduced by similar erosional conditions. These samples all imply light-tailed distributions ($\alpha \geq 2$) for both h and l values, as well as frequent removal of sub-granular lengths, with modal removal (l_{min}) and hiatus (h_{min}) values ranging from 1 to 13 µm and 3 to 21 years, respectively. Our interpretation is that, with probable long hiatuses, the bleaching depth will increase logarithmically through time (Fig. 1), passing through the depth $x_{0.5}$ corresponding to the measured erosion rate $\dot{\varepsilon}_A^M$ only briefly. Heavy-tailed distributions of removal lengths are improbable because a significant portion of the bleached depth is often removed in a single event. This requires the subsequent hiatus to be sufficiently long for $x_{0.5}$ to bleach back down to depths corresponding to $\dot{\varepsilon}_A^M \pm 2\sigma$ (Fig. 4e). By the same reasoning, l_{min} and h_{min} must co-vary to produce $\dot{\varepsilon}_A^S$ values which are consistent with $\dot{\varepsilon}_A^M$ values. The smaller l_{min} and h_{min} become, the more often a given $\dot{\varepsilon}_A^M$ will exist in nature, eventually approaching the limit of constant erosion rate assumed in Sohbati et al. (2018).

Considering all finite $\dot{\varepsilon}_A^M$ values (i.e., not XJ64-1), erosional events are expected with annual-to-decadal frequency at a scale of a few microns. By comparison, sample XJ64 seems to have lost a few cm within the past decade (Table S2). This interpretation is limited, however, by a fundamental caveat at such anomalously high erosion rates, that the corresponding t_{avg} value reduces to the order of 10^0 a (Fig. 1). This sample likely predicts a single removal event on the scale of millimeters in the past year or two. These observations are consistent with previous micro-erosion meter measurements of gneiss weathering over a period of several years which revealed polishing on the scale of microns per year with occasional loss of entire grains (Spate et al., 1995); field observations of desert varnish as well as friable surfaces on the sampled boulders (Sohbati et al., 2018); and the prediction that

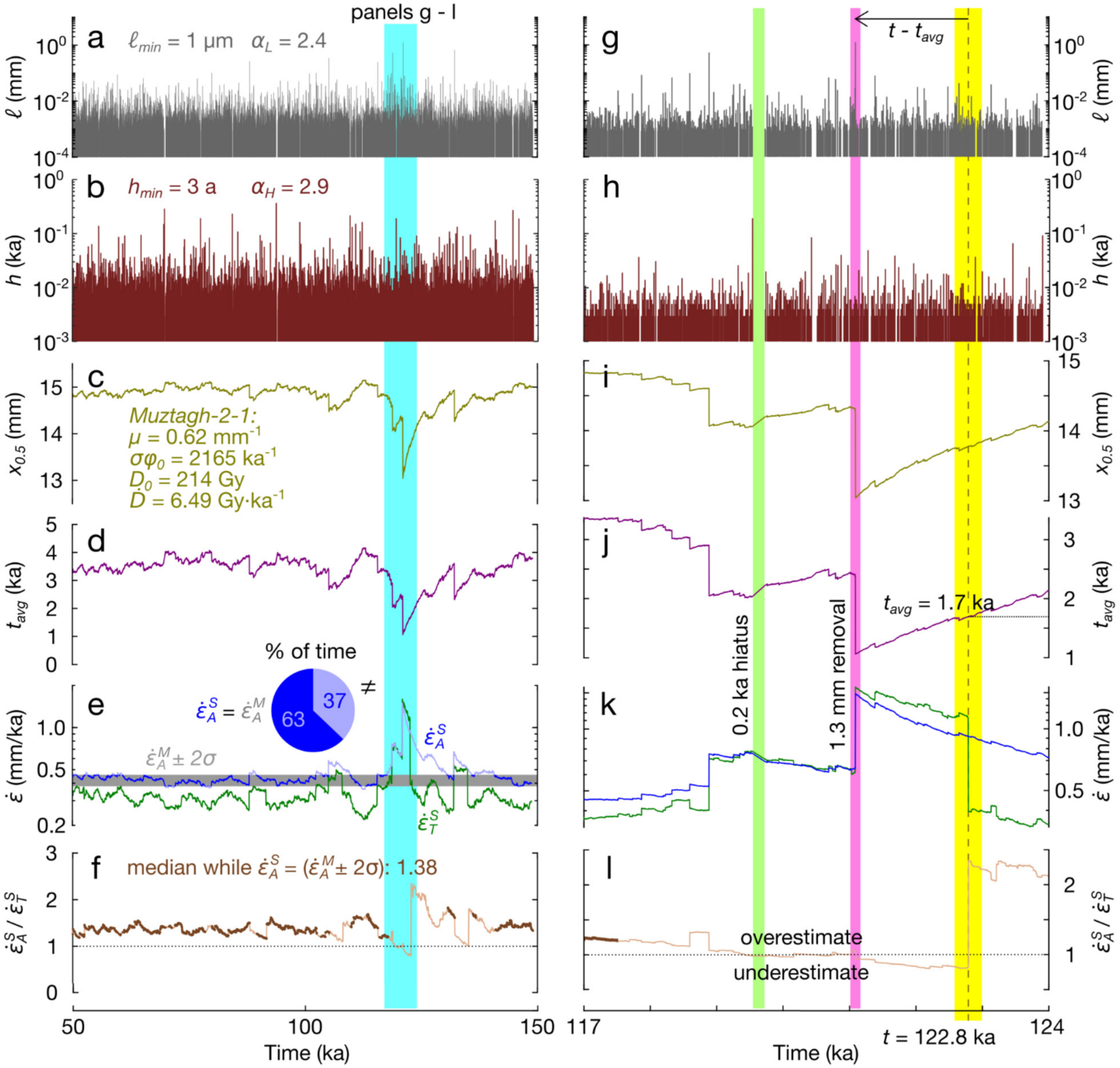

Fig. 4. The results from a stochastic erosion simulation. (a) The removal lengths l and (b) the hiatus durations h between removals are sampled from power-law distributions. (c) Based on Eq. (1), $x_{0.5}$ migrates deeper into the bedrock at a rate which depends upon four sample-specific parameters, shown in the inset. (d) The apparent averaging time t_{avg} corresponding to the apparent erosion rate $\dot{\varepsilon}_A^S$ is used to calculate the true erosion rate $\dot{\varepsilon}_T^S$, shown in panel (e). In this instance, the erosion rate measured by Sohbati et al. (2018) $\dot{\varepsilon}_A^M \pm 2\sigma$ would be observed during about 63% of the time steps, and (f) would represent a slight (median of 38%) overestimate. Panels (g)–(l) are a portion of the time series (region highlighted in light blue) and illustrate common features of these simulations, including an anomalous hiatus duration (green region) and a large removal length (pink region). In yellow, an abrupt increase in $\dot{\varepsilon}_A^S/\dot{\varepsilon}_T^S$ occurs because the large removal event t_{avg} years previously is included in $\dot{\varepsilon}_T^S$ when $t = 122.8$ ka, but not when $t = 122.8 + dt$ ka.

intra-grain microflaws often control the scale of bedrock detachment, either in response to grain impacts (Laity and Bridges, 2009) or subcritical crack propagation (Eppes and Keanini, 2017).

4.2. If erosion is stochastic, are apparent rates biased?

4.2.1. $\dot{\varepsilon}_A^S/\dot{\varepsilon}_T^S$ values

So far, we have considered which model scenarios of stochastic erosion produced apparent erosion rates ($\dot{\varepsilon}_A^S$) similar to measured erosion rates ($\dot{\varepsilon}_A^M$). Now we evaluate the accuracy of the simulated apparent erosion rates compared to the true rates ($\dot{\varepsilon}_A^S/\dot{\varepsilon}_T^S$). We consider only those time steps which produce the measured rate within 2σ and then divide that by the true erosion rate, a value obtained by dividing the total removed bedrock during the preceding t_{avg} years (Fig. 4). The results for each sample are summarized in Table S2 and Figs. S2 and 5.

The median bias for the sample XJ64-1 ($\dot{\varepsilon}_A^S = 0$–$0.04$ mm·ka^{-1}) is a 50% underestimation of the true erosion rate. When apparent erosion rates cross the threshold into being indistinguishable from 0 (e.g., $x_{0.5} >= d_{SS} - 1/\mu$; Sohbati et al., 2018), there will be a period of time with non-zero true erosion (Figs. 1 and 5c). The low median $\dot{\varepsilon}_A^S/\dot{\varepsilon}_T^S$ ratio for XJ64-1 stems from a measurement limitation. In other words, the geologist should rightly interpret the erosion rate as methodologically indistinguishable from zero, despite the fact that many times erosion will actually be finite.

For sample XJ64 ($\dot{\varepsilon}_A^M = 432 - 456$ mm·ka^{-1}), the true erosion rate is likely greater by a factor of 6.25. Given that the averaging timescale at this rate is about 1 year (Fig. 1), this measurement suggests that about 3 mm of rock was eroded about a year before

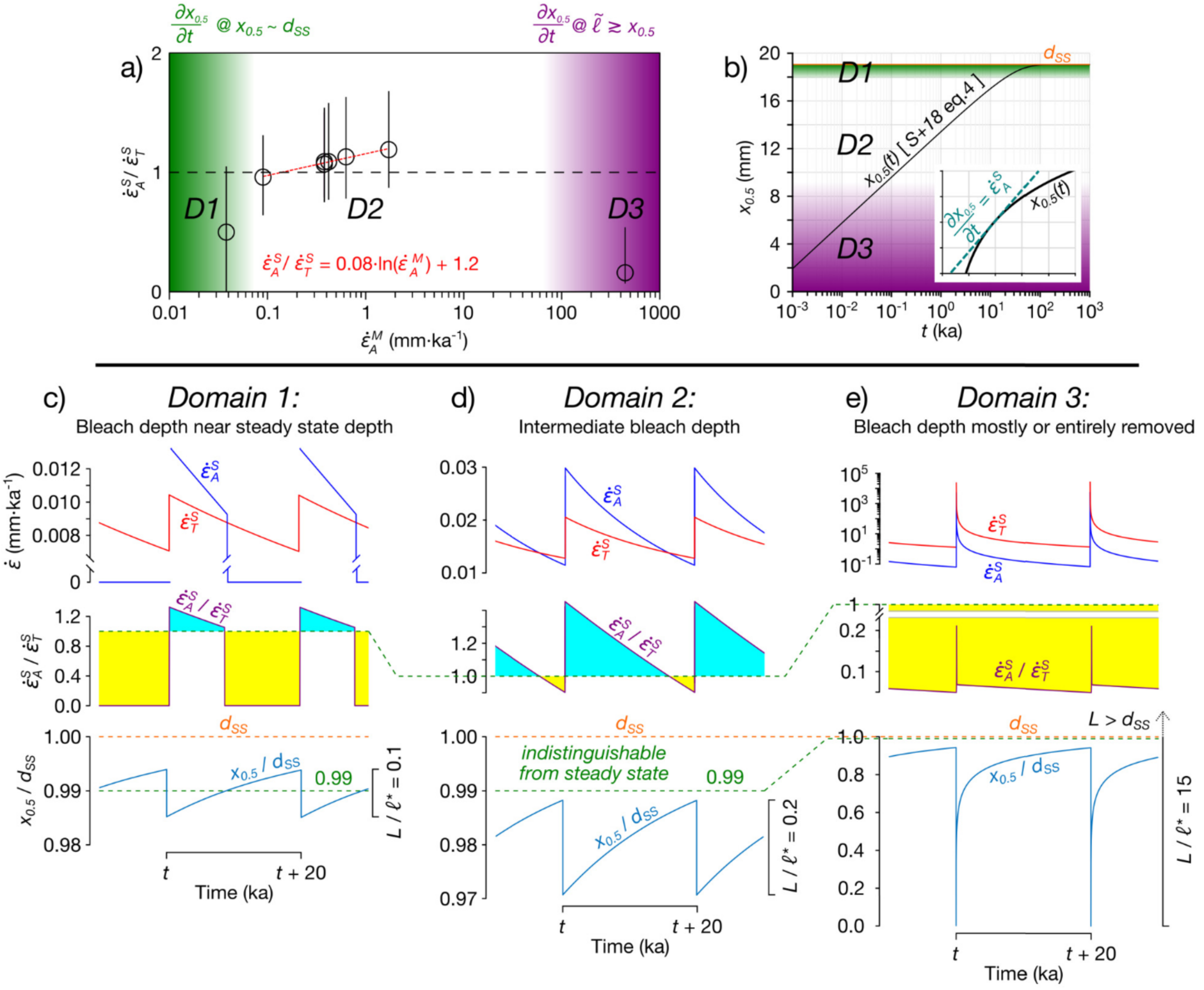

Fig. 5. (a) The range of simulated $\dot{\varepsilon}_A^S/\dot{\varepsilon}_T^S$ values are plotted as a function of the measured erosion rates $\dot{\varepsilon}_A^M$ for every sample. Circles and error bars represent the median values and interquartile ranges, respectively. (b) Measured erosion rates fall into three domains, according to bleaching depth. In Domain 1 (c), the bleaching depth often is indistinguishable from the steady-state depth without erosion. In Domain 3 (e), most or all of the bleached rock is removed during erosion. Both of these domains produce significant underestimations of erosion rates. In Domain 2 (d), erosion rate estimates are more accurate, but $\dot{\varepsilon}_A^S/\dot{\varepsilon}_T^S$ increases logarithmically as a function of the measured erosion rate.

sample collection. It is unsurprising that the predicted accuracy of this rate is poor, given that the rate does not average over many removal cycles (the number of events included in $\dot{\varepsilon}_A^S \sim (L \cdot \mu)^{-1}$; data not shown) and the majority of the bleached overburden may be removed in a single event (Fig. 5e). Sohbati et al. (2018) hypothesized that the anomalously high apparent erosion rate for XJ64 may have resulted from the discrete loss of material, invalidating an assumption of their constant erosion model.

The other six samples exhibit surprisingly accurate median $\dot{\varepsilon}_A^S/\dot{\varepsilon}_T^S$ ratios during stochastic erosion, ranging from 0.96 to 1.19. This accuracy derives from the large number of removal events contained within the t_{avg} window. For these six samples, there is a mild logarithmic increase in the median values of $\dot{\varepsilon}_A^S/\dot{\varepsilon}_T^S$ as a function of the measured erosion rate, $\dot{\varepsilon}_A^M$, caused by the rapid decrease in $\dot{\varepsilon}_A$ relative to $\dot{\varepsilon}_T$ immediately after a removal event (Fig. 5).

We note that, although our results do incorporate reported measurement errors, sources of inaccuracy other than bias related to irregular erosion are not systematically considered in the present study. For example, heterogeneous rock opacity limits the measurement reproducibility of some samples (Meyer et al., 2018; Ou et al., 2018). Recent methodological improvements (e.g., 2D rock slab imaging; Sellwood et al., 2019) continue to minimize these limitations, but future studies could detail how a rock's optical characteristics control, for example, measurable erosion regimes.

4.2.2. Controls on $\dot{\varepsilon}_A$ accuracy

To consider how removal length or hiatus duration influence accuracy, we plot $\dot{\varepsilon}_A^S/\dot{\varepsilon}_T^S$ as a function of simulation input conditions: normalized removal length $\widetilde{l}/l^*$ (Fig. 7a) and normalized hiatus duration $\widetilde{h}/h^*$ (Fig. 7b), where l^* is the mean free path (mm) of a photon into bedrock ($l^* = \mu^{-1}$), $h^* = t_{avg}(\dot{\varepsilon}_A^S)/e$, and median values are calculated from the each simulated power law distribution (Eq. (10)). Notice that a large range of l_{min} values was imposed to reproduce the high erosion rate of sample XJ64.

For all samples, $\dot{\varepsilon}_A^S/\dot{\varepsilon}_T^S$ values exhibit a negative relationship with the dimensionless erosion variables beginning near unity. As the value of $\widetilde{l}/l^*$ increases, the measured erosion rate reflects progressively fewer removal events. To recreate the same erosion rate with fewer events implies greater hiatus between removals and therefore an increased likelihood that $\dot{\varepsilon}_A^S$ following a removal will be an underestimate of $\dot{\varepsilon}_T^S$. For sample XJ64, the measured erosion

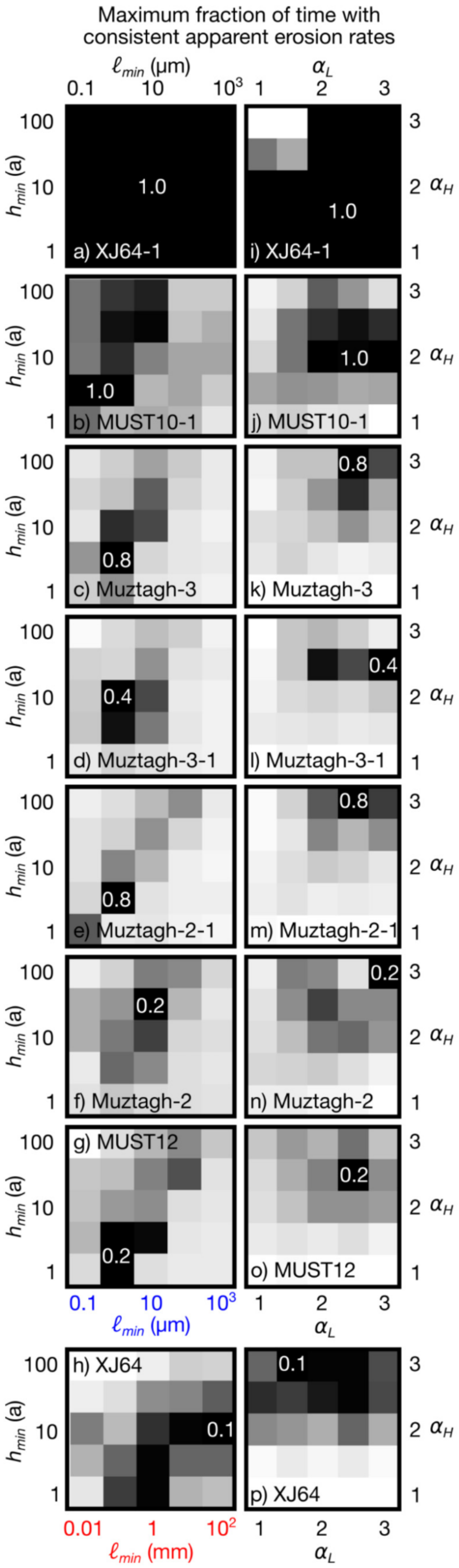

Fig. 6. Maximum fraction of time that a simulation yielded an apparent erosion rate consistent with that measured by Sohbati et al. (2018), as a function of erosional parameters l_{min} and h_{min} (panels a–h) or of α_L and α_H (panels i–p). Notice that the l_{min} scale for sample XJ64 (h) is greater than the others, which was necessary to reproduce the higher measured erosion rate.

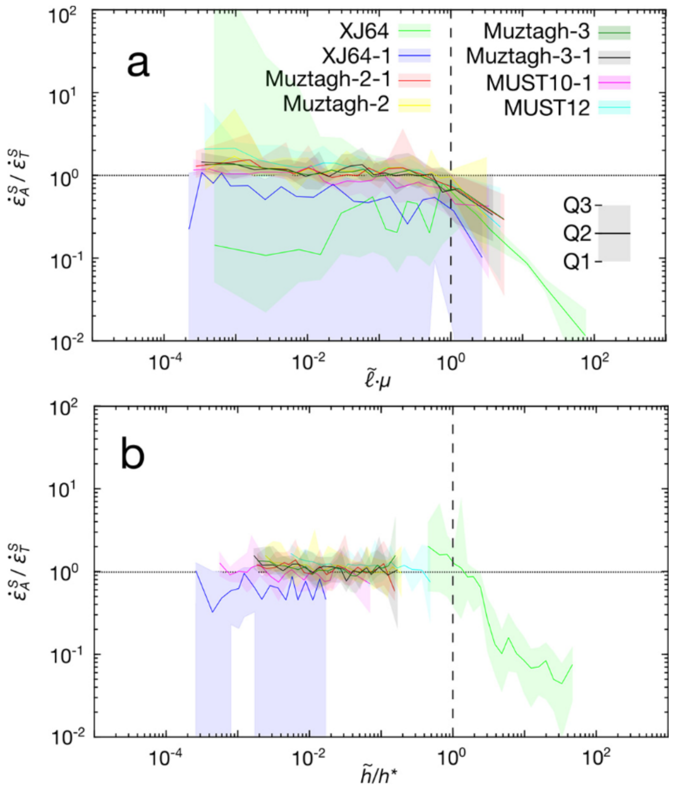

Fig. 7. The interquartile range of simulated $\dot{\varepsilon}^S_A/\dot{\varepsilon}^S_T$ values are shown as a function of dimensionless median removal length (a) and dimensionless median hiatus duration (b). When results coincide with the dotted lines, the apparent erosion rate is accurate, with regions above and below being over- and underestimations, respectively. Underestimations of erosion rates are observed when either dimensionless variable is near or greater than one (dashed line). Simulations for sample XJ64 include larger removal lengths in order to reproduce the measured erosion rate.

rate was very rarely reproduced at lower l_{min} values (see Fig. 6d), which results in significant $\dot{\varepsilon}^S_A/\dot{\varepsilon}^S_T$ variability at lower $\widetilde{l}/l^*$ values.

The reason that $\dot{\varepsilon}^S_A/\dot{\varepsilon}^S_T$ decreases without bound for increasing $\widetilde{l}/l^*$ values is that the true erosion always accounts for the removed length(s), which could be made arbitrarily large, whereas $\dot{\varepsilon}^S_A$ always derives from some finite bleaching depth $x_{0.5}$. By contrast, the apparent stabilization of $\dot{\varepsilon}^S_A/\dot{\varepsilon}^S_T$ as a function of $\widetilde{h}/h^*$ occurs because sufficiently long hiatuses reach a lower limit of resolvable $\dot{\varepsilon}_A$ values (see purple dashed line in Fig. 1b).

4.3. Identifying erosion mechanisms

We have found that measurements of erosion rates by stochastic removal are reasonably accurate over a range of rates (e.g., 0.09 to 1.72 mm·ka^{-1}). Like direct measurements of surface lowering with micro-erosion meters, this approach is sensitive to individual chipping events (Laity and Bridges, 2009), but unlike direct measurements, these rates are integrated over many removal events (cf. Spate et al., 1995). By subsampling ventifacts in high spatial density, this approach could be used to more directly estimate the variability of removal lengths and thereby monitor, for example, the height dependence of erosion by saltating grains (Anderson and Hallet, 1986; Bridges and Laity, 2013). The hardness of crystalline rock has made this measurement particularly difficult to observe directly (Rohrmann et al., 2013).

Having examined the reliability of measured erosion rates, we now consider how true erosion rates are predicted to vary between ground-level and boulder-top (diameter >2 m) samples of Sohbati et al. (2018). At each of the field sites, a pair of rock samples was collected: one from a ground-level rock surface and one

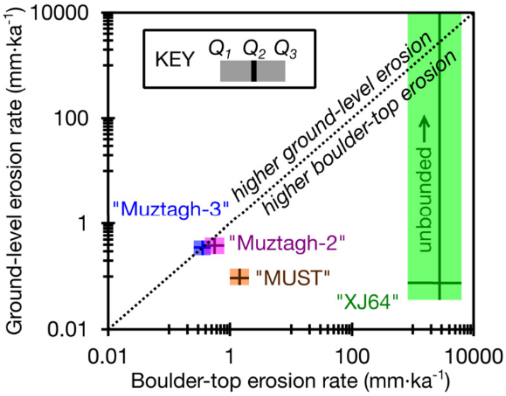

Fig. 8. At each of the four field sites, Sohbati et al. (2018) collected one sample at the ground surface and one atop large (>2 m tall) boulders. These pairs are plotted for each field site to compare ground-level and boulder-top erosion rates. The simulated interquartile ranges for true erosion rates are shown as the shaded rectangles.

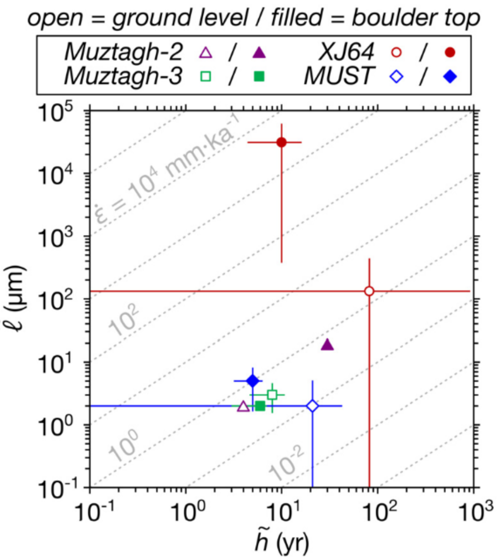

Fig. 9. Median erosion length $\tilde{l}$ and hiatus $\tilde{h}$ are shown for ground-level and boulder-top samples. The values shown here are the most likely input parameters listed in Table S2. Notice that $\tilde{l}$ values from boulder-top samples are similar to or greater than values at ground level.

atop a large boulder. Each pair has therefore likely experienced the same precipitation, sand storms, freeze-thaw cycles, and so on. At all four sites the boulder-top erosion rates and median removal lengths are greater than or equal to the ground-level rates and lengths (Figs. 8 and 9). The erosional length scales predicted for both ground-level and all but one of the boulder-top samples (10^0–10^2 µm) are similar to those produced by subcritical cracking, a process promoted by full daylight exposure and other environmental stresses (Eppes et al., 2016; Eppes and Keanini, 2017; Eppes et al., 2018). Sample XJ64, a boulder-top sample, is the exception, with a predicted loss of several mm within the last several years, consistent with observations of physical weathering processes such as rock spalling or flaking (Spate et al., 1995). Considering the aridity of the region (Owen et al., 2012; Song et al., 2016) and the absence of deeply pitted surfaces (Sohbati et al., 2018), the influence of chemical weathering is probably limited at these sites. In addition, if aeolian abrasion were dominant, erosion rates should be highest within a few decimeters of the surface and negligible at boulder tops (Bridges and Laity, 2013). Our observations of higher boulder-top erosion rates and greater removal lengths are more consistent with mechanical weathering such as subcritical cracking or exfoliation, rather than chemical weathering or aeolian abrasion, as the dominant mechanism for bedrock erosion in this area.

5. Conclusions

Luminescence profiles in bedrock inform the geologist about erosional characteristics on centennial-to-millennial timescales. We have shown that at low rates (10^{-1}–10^1 mm·ka^{-1}) this measurement is surprisingly accurate, even with stochastic erosion. Simulation results indicate that heavy-tailed distributions of removal length or hiatus duration are unlikely to produce the measured luminescence bleaching profiles. At higher rates (10^2–10^3 mm·ka^{-1}), the bleaching depth is sensitive to individual rock chipping events. For example, for the sample with the greatest apparent erosion, we estimate that several mm of rock probably flaked off during the past few years. We hope that these findings encourage the collection of new datasets to better understand bedrock erosion mechanisms at the granular scale in a variety of environments.

Acknowledgements

Thanks to Raleigh Martin and Jasper Kok for helpful discussions about aeolian abrasion and to Harrison Gray and another anonymous reviewer for their insightful comments. We gratefully acknowledge support from NSF-EAR-1728145 and NSF-EAR-1806629.

Appendix A. Supplementary material

Supplementary material related to this article can be found online at https://doi.org/10.1016/j.epsl.2019.115842.

References

Anderson, R.S., Hallet, B., 1986. Sediment transport by wind: toward a general model. Geol. Soc. Am. Bull. 97, 523–535.
Bierman, P.R., Caffee, M., 2002. Cosmogenic exposure and erosion history of Australian bedrock landforms. Geol. Soc. Am. Bull. 114, 787–803.
Bridges, N.T., Laity, J.E., Greeley, R., Phoreman, J., Eddlemon, E.E., 2004. Insights on rock abrasion and ventifact formation from laboratory and field analog studies with applications to Mars. Planet. Space Sci. 52, 199–213.
Bridges, N.T., Laity, J.E., 2013. Fundamentals of aeolian sediment transport: aeolian abrasion. In: Lancaster, N., Sherman, D.J., Baas, A.C.W. (Eds.), Treatise on Geomorphology, vol. 11. Academic Press, pp. 134–148.
Clauset, A., Shalizi, C.R., Newman, M.E.J., 2009. Power-law distributions in empirical data. Soc. Ind. Appl. Math. 51, 661–703.
Emmanuel, S., Levenson, Y., 2014. Limestone weathering rates accelerated by micron-scale grain detachment. Geology 42, 751–754.
Eppes, M.C., Hancock, G.S., Chen, X., Arey, J., Dewers, T., Huettenmoser, J., Kiessling, S., Moser, F., Tannu, N., Weiserbs, B., Whitten, J., 2018. Rates of subcritical cracking and long-term erosion. Geology 46, 951–954.
Eppes, M.C., Keanini, R., 2017. Mechanical weathering and rock erosion by climate-dependent subcritical cracking. Rev. Geophys. 55, 470–508.
Eppes, M.C., Magi, B., Hallet, B., Delmelle, E., Mackenzie-Helnwein, P., Warren, K., Swami, S., 2016. Deciphering the role of solar-induced thermal stresses in rock weathering. Geol. Soc. Am. Bull. 128, 1315–1338.
Finnegan, N.J., Schumer, R., Finnegan, S., 2014. A signature of transience in bedrock river incision rates over timescales of 10^4–10^7 years. Nature 505, 391–394.
Ganti, V., von Hagke, C., Scherler, D., Lamb, M.P., Fischer, W.W., Avouac, J.P., 2016. Time scale bias in erosion rates of glaciated landscapes. Sci. Adv. 2, e1600204.
Gardner, T.W., Jorgensen, D.W., Shuman, C., Lemieux, C.R., 1987. Geomorphic and tectonic process rates: effects of measured time interval. Geology 15, 259–261.
Gilbert, G.K., 1877. Geology of the Henry Mountains. Technical Report. USGS.
Granger, D.E., Riebe, C.S., 2014. Cosmogenic nuclides in weathering and erosion. In: Treatise on Geochemistry, second edition. Elsevier, Amsterdam, pp. 402–436.
Jerolmack, D.J., Reitz, M.D., Martin, R.L., 2011. Sorting out abrasion in a gypsum dune field. J. Geophys. Res. 116, F02003.
Kirchner, J.W., Finkel, R.C., Riebe, C.S., Granger, D.E., Clayton, J.L., King, J.G., Megahan, W.F., 2001. Mountain erosion over 10 yr, 10 k.y., and 10 m.y. time scales. Geology 29, 591–594.
Laity, J.E., Bridges, N.T., 2009. Ventifacts on Earth and Mars: analytical, field, and laboratory studies supporting sand abrasion and windward feature development. Geomorphology 105, 202–217.
Lal, D., 1991. Cosmogenic ray labeling of erosion surfaces: in situ nuclide production rates and erosion models. Earth Planet. Sci. Lett. 104, 424–439.

Meyer, M.C., Gliganic, L.A., Jain, M., Sohbati, R., Schmidmair, D., 2018. Lithological controls on light penetration into rock surfaces–implications for OSL and IRSL surface exposure dating. Radiat. Meas. 120, 298–304.

Moses, C., Robinson, D., Barlow, J., 2014. Methods for measuring rock surface weathering and erosion: a critical review. Earth-Sci. Rev. 135, 141–161.

Muzikar, P., 2008. Cosmogenic nuclide concentrations in episodically eroding surfaces: theoretical results. Geomorphology 97, 407–413.

Muzikar, P., 2009. General models for episodic surface denudation and its measurement by cosmogenic nuclides. Quat. Geochronol. 4, 50–55.

Niemi, N.A., Oskin, M., Burbank, D.W., Heimsath, A.M., Gabet, E.J., 2005. Effects of bedrock landslides on cosmogenically determined erosion rates. Earth Planet. Sci. Lett. 237, 480–498.

Ou, X.J., Roberts, H.M., Duller, G.A.T., Gunn, M.D., Perkins, W.T., 2018. Attenuation of light in different rock types and implications for rock surface luminescence dating. Radiat. Meas. 120, 305–311.

Owen, L.A., Chen, J., Hendrick, K.A., Caffee, M.W., Robinson, A.C., Schoenbohm, L.M., Yuan, Z., Imrecke, D.B., Liu, J., 2012. Quaternary glaciation of the Tashkurgan valley, Southeastern Pamir. Quat. Sci. Rev. 47, 56–72.

Perron, J.T., 2017. Climate and the pace of erosional landscape evolution. Annu. Rev. Earth Planet. Sci. 45, 561–591.

Portenga, E.W., Bierman, P.R., 2011. Understanding Earth's eroding surface with ^{10}Be. GSA Today 21, 4–10.

Portenga, E.W., Bierman, P.R., Rizzo, D.M., Rood, D.H., 2013. Low rates of bedrock outcrop erosion in the central Appalachian Mountains inferred from in situ ^{10}Be. Geol. Soc. Am. Bull. 125, 201–215.

Rohrmann, A., Heermance, R., Kapp, P., Cai, F., 2013. Wind as the primary driver of erosion in the Qaidam Basin, China. Earth Planet. Sci. Lett. 374, 1–10.

Sadler, P.M., 1981. Sediment accumulation rates and the completeness of stratigraphic sections. J. Geol. 89, 569–584.

Schumer, R., Jerlomack, D.J., 2009. Real and apparent changes in sediment deposition rates through time. J. Geophys. Res. 114, F00A06.

Sellwood, E.L., Guralnik, B., Kook, M., Prasad, A.K., Sohbati, R., Hippe, K., Wallinga, J., Jain, M., 2019. Optical bleaching front in bedrock revealed by spatially-resolved infrared photoluminescence. Sci. Rep. 9, 2611.

Small, E.E., Anderson, R.S., Repka, J.L., Finkel, R., 1997. Erosion rates of Alpine bedrock summit surfaces deduced from in situ ^{10}Be and ^{26}Al. Earth Planet. Sci. Lett. 150, 413–425.

Sohbati, R., Jain, M., Murray, A., 2012. Surface exposure dating of non-terrestrial bodies using optically stimulated luminescence: a new method. Icarus 221, 160–166.

Sohbati, R., Liu, J., Jain, M., Murray, A., Egholm, D., Paris, R., Guralnik, B., 2018. Centennial- to millennial-scale hard rock erosion rates deduced from luminescence-depth profiles. Earth Planet. Sci. Lett. 493, 218–230.

Sohbati, R., Murray, A., Jain, M., Buylaert, J.P., Thomsen, K., 2011. Investigating the resetting of OSL signals in rock surfaces. Geochronometria 38, 249–258.

Song, H., Zhang, K., Piao, S., Wan, S., 2016. Spatial and temporal variations of spring dust emissions in northern China over the last 30 years. Atmos. Environ. 126, 117–127.

Spate, A.P., Burgess, J.S., Shevlin, J., 1995. Rates of rock surface lowering, Princess Elizabeth Land, Eastern Antarctica. Earth Surf. Process. Landf. 20, 567–573.

Viles, H.A., 2012. Microbial geomorphology: a neglected link between life and landscape. Geomorphology 157, 6–16.

Wright, J., Smith, B., Whalley, B., 1998. Mechanisms of loess-sized quartz silt production and their relative effectiveness: laboratory simulations. Geomorphology 23, 15–34.

Yanites, B.J., Tucker, G.E., Anderson, R.S., 2009. Numerical and analytical models of cosmogenic radionuclide dynamics in landslide-dominated drainage basins. J. Geophys. Res. 114, 1–20.